Electronic Supplementary Material (ESI) for Physical Chemistry Chemical Physics.

Electronic Supplementary Information

Molecular insight into carboxylic acid - alkali metal cations interactions: reversed affinities and ion-pair formation revealed by non-linear optics and simulations.

Adrien Sthoer,[†] Jana Hladílková,[‡] Mikael Lund,[‡] and Eric Tyrode[*†]

[†]*Department of Chemistry, KTH Dröttning Kristinas väg 51, SE-10044 Stockholm, Sweden*
[‡]*Division of Theoretical Chemistry, Lund University, P.O.B. 124, SE-22100 Lund, Sweden*

Corresponding author: tyrode@kth.se

Content:

1. **Detection of polyvalent ion impurities in monovalent salts by vibrational sum frequency spectroscopy.**

Although previous VSFS studies on monovalent ion interactions with a fatty acid Langmuir monolayer, have considered the influence of potential organic impurities in the salts used,[1, 2] the effect of trace ion contamination in high purity salts has never been addressed.

Figure S1a shows repeat VSF experiments of deuterated arachidic acid monolayers on 1 M NaCl solutions in the absence of EDTA in the subphase. The salt was high purity NaCl (99.999% trace metal analysis, Sigma-Aldrich) that had been baked at 500°C before use. The spectra in the carboxylate stretching region is highly irreproducible (Figure S1). These variations were independent of the salt batch used, with changes observed even for solutions prepared from the same salt container. At least four symmetric carboxylate bands are identified in the spectra. They are centred at 1408 cm^{-1}, 1435 cm^{-1}, 1445 cm^{-1}, and 1475 cm^{-1}. The three bands at higher frequencies are associated to the formation of polyvalent metal - carboxylate complexes.[3, 4] The overall intensity of these bands is higher than those reported in the main article in the presence of EDTA, as divalent and trivalent ions will further promote the deprotonation of the monolayer. For example, when the 1445 cm^{-1} and/or 1475 cm^{-1} bands are present in the spectrum, the carbonyl signal at 1720 cm^{-1} decreases significantly, indicating a relatively lower proportion of uncharged carboxylic acids groups in the corresponding monolayers.

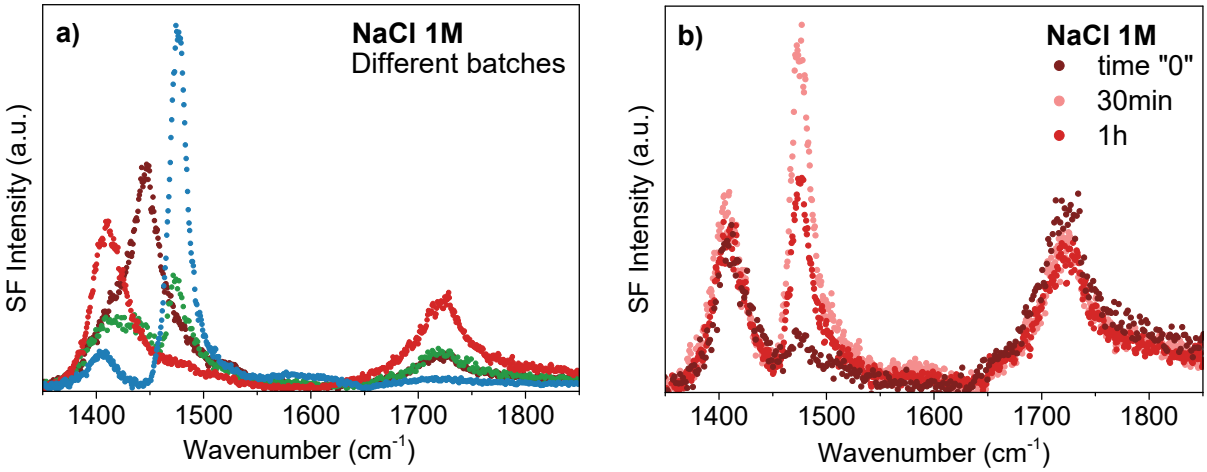

Figure S1 – VSF spectra of a dAA monolayer collected in the SSP polarization combination at 22°C and pH=6 for different batches of NaCl salts (*a*), and as a function of time (*b*).

The spectral features linked to the state of complexation also exhibited time-dependent variations as shown in Figure S1b. At time "zero" the hydrated carboxylate stretch at 1408 cm^{-1} dominates the spectrum. However, 1 hour later it is the 1475 cm^{-1} peak associated with a multivalent cation-carboxylate complex that prevails. This behavior is characteristic of a diffusion-controlled adsorption mechanism, expected for trace metal ions in the ppm to ppb concentration range. We note that a similar time-dependent behavior was reported by Tang et al.[5] for Na^+ and K^+ ions interacting with a palmitic

acid monolayer, which in the light of the work presented here, was incorrectly interpreted as K^+ having a higher propensity to bind to the carboxylate headgroup.

The appearance of multiple bands in the carboxylate stretching region was not limited to NaCl, as the same behavior was observed, for example, for CsCl (99.999% trace metal analysis) and LiCl (99.99% trace metal analysis) as shown in Figure S2a. Upon introduction of EDTA in submicromolar concentrations to the subphase, only the hydrated carboxylate stretch at 1408 cm^{-1} remains as shown in Figure S2b (red spectrum). The spectra become then reproducible and time independent.

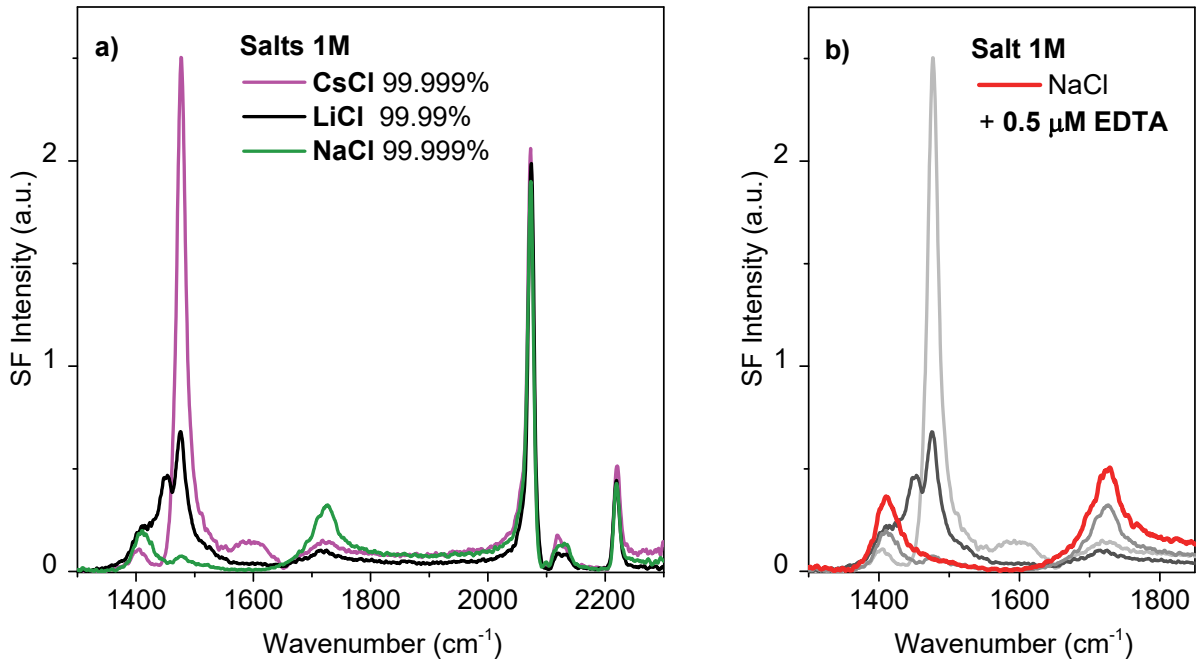

Figure S2 – VSF spectra of dAA monolayer collected in the SSP polarization combination at 22 °C and pH~6 on (a) 1M NaCl, LiCl and CsCl subphase in the absence of EDTA, and (*b*) NaCl after addition of 0.5 µM EDTA to the subphase.

EDTA is a soluble chelating agent widely used in biochemistry to remove traces of polyvalent impurities in monovalent salt solutions. EDTA, consisting of four carboxylic acid groups with four acidity constants[6] (pK_{a1} 2.00; pK_{a2} 2.67; pK_{a3} 6.16; pK_{a4} 10.26), shows high binding affinities to polyvalent cations. The equilibrium constants for the formation of complexes with different cations in solution are summarized in Table S1. The stability constants are significantly lower for the alkali metal cations when compared with selected divalent and trivalent cations, which are commonly present in trace amounts in high purity salt used (in the ppb and ppm range). Table S1 shows that the EDTA affinities for divalent and trivalent ions are 10 to 20 order of magnitude higher than for monovalent cations. Thus, EDTA can very effectively remove trace multivalent ions from solution, even in the presence of an overwhelmingly larger amount of monovalent cations.

Table S1 – Stability constants of EDTA complexes with alkali metal cations and typical divalent and trivalent cations found in trace amounts in the high purity salts used.
The values presented correspond to log $K_{metal\text{-}ligand}$ (pK_{ML}) [6]

Cation	Range of stability constant with EDTA
Li^+	2.79 (20°C)
Na^+	1.66 (20°C)
K^+	0.55 (25°C)
Cs^+	0.15 (25°C)
Ca^{2+}	10.7 (20°C)
Fe^{2+}	14.3 (20°C)
Fe^{3+}	25.1 (20°C)
Y^{3+}	18.11 (20°C)
La^{3+}	15.5 (20°C)

EDTA has a relatively high solubility in water (solubility limit of 1.37 mM at neutral pH and at 20°C) and does not affect the pH when present at concentrations below 1 µM. At higher concentrations, EDTA lowers the pH of the solution (up to pH 4.5 for 20 µM of EDTA). The amount of EDTA required to remove trace divalent and trivalent ions varied depending on the salt batch used, but concentration ≤20 µM was typically sufficient for most cases. Note that for a 99.999% purity salt the amount of trace metals is typically specified as ≤ 15 ppm, while for a 99.98% purity salt this value raises to ≤ 250 ppm. This is equivalent in a 1 M solution to 15 µM, and 250 µM of trace metals, respectively. In this sense, salts of the highest purity available are preferred. Nonetheless, the most relevant point is the total amount and identity of the divalent and, in particular, trivalent ions in solution, which could vary significantly from batch to batch (including the same salt container).

Additionally, EDTA is not surface active and consequently does not disturb the fatty acid monolayer. This was proven by surface tension measurements, where a 1 mM EDTA solution showed, within error, the same surface tension values as for pure water. VSFS also shows that the packing of the fatty acid alkyl chain is not affected by the presence of EDTA (Figure S3a), with no signs of CH stretching modes when measuring the SF spectrum of a dAA monolayer on 1 M NaCl subphase containing EDTA (Figure S3b).

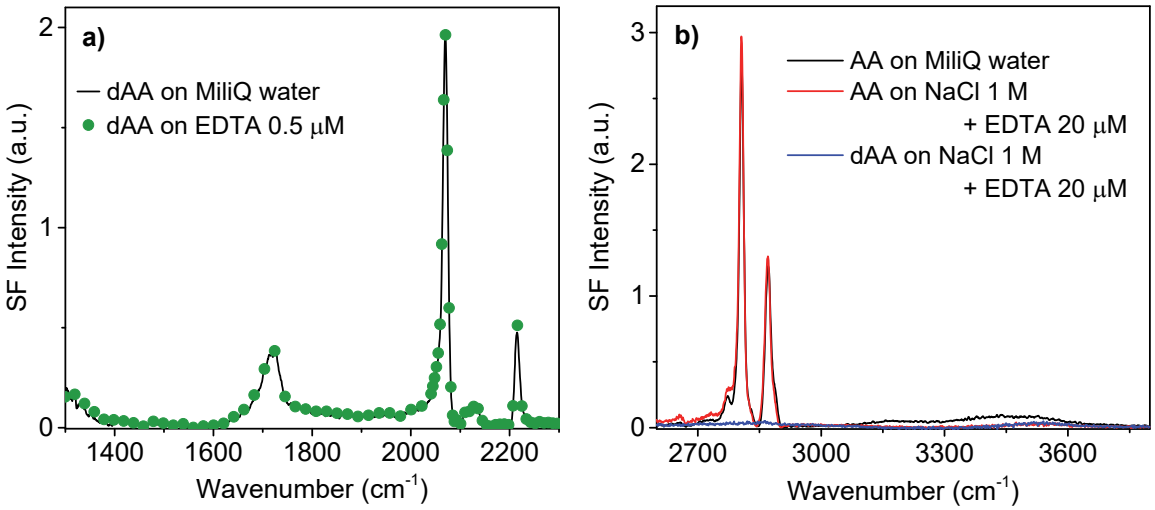

Figure S3 – VSF SSP spectra of dAA on (*a*) a pure water subphase and 0.5 μM EDTA solution head group and CD stretching region, and (*b*) on a 1M electrolyte solution containing 20 μEDTA in the CH and OH stretching region.

2. Determining the Raman depolarization ratio of the C=O stretch.

The Raman spectra used for determining the depolarization ratio of the carbonyl band were collected in a home-built spectrometer described in detail elsewhere.[7] Briefly, a 532 nm CW laser (Laser Quantum, UK) of ~2 mm in diameter is focused on the sample position with a Gradium lens (focal length 80 mm). The sample is placed in a sealed transparent glass tube of 4 mm in diameter. The scatter light is collected in a close to 90° configuration using an ultra-long working distance objective (M-Plan Apo 50X, NA 0.55, Mitutoyo, Japan) and detected using a spectrometer / CCD camera (Shamrock 303i, Newton DU940N-BV, Andor, Ireland).

To determine the depolarization ratio of the carbonyl group, polarized Raman spectra parallel ($I_{\parallel}$) and perpendicular ($I_{\perp}$) to the polarization plane of the exciting laser were collected for a 250 mM butyric acid solution (see Figure S4). Diluted acid solutions were used to make certain the carboxylic acid was found in its hydrated form, as dimeric species are expected at high concentrations. In Figure S4, the vibrational mode at ~1715 cm^{-1} is assigned to the carbonyl stretch of the hydrated carboxylic acid.[8] The spectra were fitted to Gaussian lines shapes resulting in the parameters summarized in Table S2. The depolarization ratio (ρ) of the carbonyl group, defined as $\rho = I_{\perp} / I_{\parallel}$, was found to be:

$$\rho = \frac{I_{\perp}}{I_{\parallel}} = 0.11 \pm 0.005$$

Table S2 – Fitting parameters for the carbonyl peak.

	$I_{\perp}$	I_{II}
ν_s frequency	1715 cm^{-1}	1715 cm^{-1}
Amplitude	2.42 E+4	2.08 E+5
FWHM	55	55

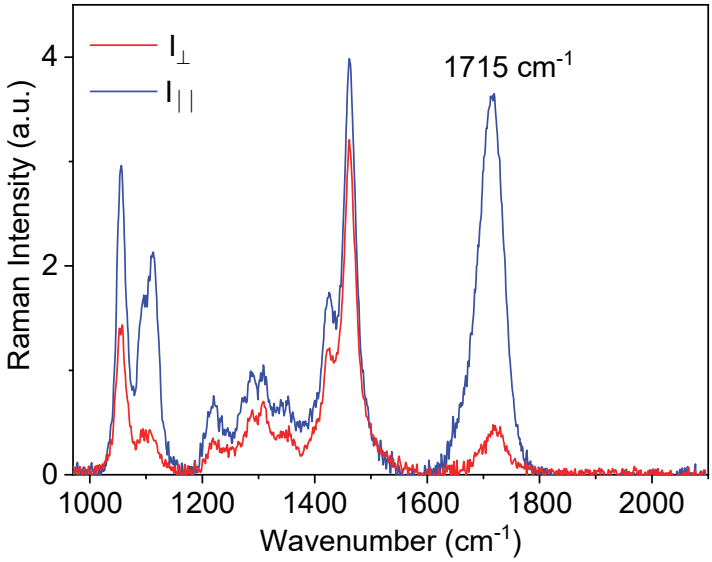

Figure S4 – Raman spectra polarized parallel ($I_{\parallel}$) and perpendicular ($I_{\perp}$) to the polarization plane of the exciting laser of a 250 mM aqueous butyric acid solution. Spectra had previously been subtracted from those of pure water to remove contributions from the solvent. Excitation source: 532 nm CW 300 mW laser. Details of the spectrometer can be found elsewhere.[9]

3. Accounting for ion steric effects in double layer models: modified Poisson Boltzmann.

The Poisson Boltzmann theory (PB) describes the distribution of ions near a charged interface by taking into account the electrostatic potential, and an entropic contribution opposed to the packing of the charge particles in the diffuse layer. In the classical model, ions in solution are considered as point-like charges interacting in a mean field potential. The concentration profile of ions is given by a statistical Boltzmann distribution (Equation 1).[10] Combining the charge distribution profile with the Poisson equation leads to the Poisson-Boltzmann equation (Equation 2). Gouy[11] and Chapman[12] independently proposed an analytical solution for a 1:1 electrolyte, and the special boundary condition relating the surface charge to the surface potential known as the Gouy-Chapman equation (Equation S3):

$$C_{i(x)} = C_{i(\infty)} e^{-\frac{z_i e \psi_{(x)}}{kT}} \qquad [S1]$$

$$\nabla^2 \psi_{(x)} = -\frac{e}{\varepsilon \varepsilon_0} \sum_i z_i C_{i(\infty)} e^{-\frac{z_i e \psi_{(x)}}{kT}} \qquad [S2]$$

$$\psi_0 = \frac{2kT}{e}\sinh^{-1}\left\{\frac{\sigma}{\sqrt{8kTC_\infty\varepsilon\varepsilon_0}}\right\} \text{ (for a 1:1 electrolyte)} \quad [S3]$$

where C_∞ is the bulk ion concentration, e the elementary charge, z_i the valence of the ion i, ε and ε_0 the permittivity of the medium and vacuum, ψ_0 the electrostatic potential at the surface, and σ the surface charge density.

Prediction of the monolayer deprotonation.

The dissociation of the acid group in the monolayer can be expressed as:[13]

$$RCOOH \leftrightarrow H^+ + RCOO^-$$

$$K_a = \frac{\left[H^+\right]_0\left[A^-\right]_0}{\left[HA\right]_0} = \frac{\alpha}{1-\alpha}\left[H^+\right]_0 \quad [S4]$$

where, K_a is the acidity constant, α the fraction of dissociation of the acid, and the subscript "0" refers to the surface location. The surface concentration of hydronium ions ($[H^+]_0$) is related to that in the bulk ($[H^+]_\infty$) by the surface potential (ψ_0):[14]

$$\left[H^+\right]_0 = \left[H^+\right]_\infty e^{-e\psi_0/kT} \quad [S5]$$

$$K_a = \frac{\alpha}{1-\alpha}\left[H^+\right]_\infty e^{-e\psi_0/kT} \quad [S6]$$

$$\frac{1-\alpha}{\alpha} = \frac{\left[H^+\right]_\infty}{K_a}e^{-e\psi_0/kT} \Rightarrow \ln\left(\frac{1-\alpha}{\alpha}\right) = \ln\left[H^+\right]_\infty - \ln K_a - \frac{e\psi_0}{kT} \quad [S7]$$

$$\psi_0 = \frac{kT}{e}\left[\ln\left[H^+\right]_\infty - \ln K_a - \ln\left(\frac{1-\alpha}{\alpha}\right)\right] \quad [S8]$$

The surface charge density of the monolayer (σ) is related to the surface potential by equation S3, and can be expressed as a function of the known area per molecule (A_M) and degree of deprotonation (α):

$$\sigma = \frac{\alpha e}{A_M} \quad [S9]$$

Combining equations S3, S8 and S9 results in equation S10 that allows calculating the degree of deprotonation as a function of the electrolyte concentration and hydronium ion concentration in the bulk:

$$\sqrt{C_\infty} = \frac{\alpha e}{A_M \sqrt{8\varepsilon\varepsilon_0 kT}} \left\{ \sinh\left(\frac{1}{2} \left(\ln\left[H^+\right]_\infty - \ln K_a - \ln\left(\frac{\alpha}{1-\alpha} \right) \right) \right) \right\}^{-1} \quad [S10]$$

Modified Poisson Boltzmann (MPB) model accounting for steric effects

For monovalent ion concentrations exceeding 50 mM, and/or surface potential >250 mV, the fundamental assumptions of the Poisson Boltzmann theory are no longer valid. In particular, the predicted ion concentrations at the surface exceed what is physically possible, and the finite size of the ions need to be taken into account to correctly predict the surface potential and distribution of ions near the interface.[15, 16] This can be accomplished using a modified Poisson Boltzmann model (MPB) that considers steric effects by introducing the packing parameter ν (Equation S11), that depends on a, a fitting parameter linked to the effective ion size.[15, 17]

$$\nu = 2a^3 C_\infty \quad [S11]$$

Taking into account the steric correction, the Boltzmann distribution for cations as a function of the bulk ion concentration C_∞, is written instead as:

$$C_{(x)} = \frac{C_\infty e^{\frac{-e\psi_{(x)}}{kT}}}{1 + 2\nu \sinh^2\left(\frac{e\psi_{(x)}}{2kT} \right)} \quad [S12]$$

The MPB equation is solved using the same boundary conditions as for the PB equation: $\psi_{(x=0)} = \psi_0$, $\psi_{(x\to\infty)} = 0$, $d\psi/dx_{(x\to\infty)} = 0$, leading to an expression that relates the surface charge density (σ) to the surface potential, which for a 1:1 electrolyte results in: [16]

$$\sigma^2 = \frac{4\varepsilon\varepsilon_0 kTC_\infty}{\nu} \ln\left[1 + 2\nu \sinh^2\left(\frac{e\psi_0}{2kT} \right) \right] \quad [S13]$$

or alternatively, when solving for the surface potential as:

$$\psi_0 = \frac{2kT}{e} \sinh^{-1} \sqrt{\frac{1}{2\nu} \left(\exp\left(\frac{\nu\sigma^2}{4\varepsilon\varepsilon_0 kTC_\infty} \right) - 1 \right)} \quad [S14]$$

The monolayer deprotonation as a function of pH and surface potential can be described following the same procedure used above for the Gouy-Chapman model (Equations S4 to S8). Note that when expressing the hydronium ion concentration at the surface (Equation S5), we neglect the correction accounting for the specific size of the hydrated proton (denominator in Equation S11) and assume a classical Boltzmann distribution for the proton. This is justified given low proton concentrations in

solution that the surface potentials do not exceed 0.5 V. Equating equation S14 to S8, and solving for the bulk alkali metal cation concentration results in Equation S15, which is also Equation 4 in the main text:

$$\sqrt{C_\infty} = \sqrt{\frac{\exp\left(\frac{e^2\alpha^2 a^3}{2A_M^2 \varepsilon\varepsilon_0 kT}\right)-1}{4a^3}} \cdot \left\{\sinh\left[\frac{1}{2}\left(\ln\left[H^+\right]_\infty - \ln K_a - \ln\left(\frac{\alpha}{1-\alpha}\right)\right)\right]\right\}^{-1} \qquad [S15]$$

Fitting our data at pH 6.0 (Figure 2) with equation S15 gives dimensional parameters a = 7.5 Å for CsCl, a = 7.5 Å for NaCl, and a = 9 Å for LiCl (+/- 0.2 Å). The fitted parameter "a" is associated with a characteristic size of the ion, accounting for the ionic hard sphere, its hydration shell, and possibly lateral interactions. These values are in the right order of magnitude and qualitatively consistent with hydrated cation diameters.

4. Parametrization of the coarse grained model and results from all-atom MD simulations using other tested force fields.

To parametrize ion-ion and ion-COO^- interactions, experimental activity coefficients of relevant salts were used. Epsilon values of the Lennard-Jones interaction potential were kept constant for all salts (ε = 0.05 kJ/mol) while sigma values (σ) were adjusted to reproduce activity coefficients in the range of 100 mM to 1 M of the following salts: LiCl, NaCl, CsCl, CH_3COOLi, CH_3COONa, CH_3COOCs. No experimental values were available for the interactions of cations with the carboxylic acid. Therefore, the sizes (σ) from the chloride salts were kept and the depths of the interaction (ε) were adjusted based on all-atom simulations with the van der Vegt's force field.[18] All obtained parameters are specified in Table S3.

Table S3 – Sigma and epsilon values of Lennard-Jones interactions used in coarse grained grand canonical Monte Carlo simulations. Experimental mean activity coefficients, γ, for salts at 1 M concentration are from ref.[19]

	$\gamma_{(X\text{-}Cl)}$	σ (X-Cl) [Å]	ε (X-Cl) [kJ/mol]	σ (X-COOH) [Å]	ε (X-COOH) [kJ/mol]	$\gamma_{(X\text{-}COO^-)}$	σ (X-COO-) [Å]	ε (X-COO-) [kJ/mol]
Li^+	0.744	4.66	0.05	4.96	0.05	0.689	4.01	0.05
Na^+	0.657	3.99	0.05	4.29	0.5	0.757	4.74	0.05
Cs^+	0.544	2.92	0.05	3.22	1.2	0.802	5.06	0.05

Charmm36 force field describing the monolayer was tested for comparison of the structural features to the OPLS force field and the experiment. The orientation of the carbonyl group (C=O) of the acid

relative to the surface normal was calculated as a function of the deprotonation degree of the monolayer (see Figure S5). One-peak distribution, with an exception of a small shoulder at 0 % deprotonation, was obtained. A peak shift further from the surface plane was also observed (67° → 65°) but much smaller than with the OPLS force field (83° → 73°).

An ionic force field implicitly accounting for ion polarization[20, 21] was also tested in order to determine the amount of cations at the surface as a function of the monolayer deprotonation. The same qualitative results were obtained as with the van der Vegt's force field.[18] Comparing the cations at Figure S6, we observe that the preferential interaction follows $Cs^+ > Na^+ > Li^+$ in the range 0 – 20 % of the monolayer deprotonation. The Hofmeister swap is then identified and at high degrees of deprotonation the reversed series is seen $Li^+ \geq Na^+ > Cs^+$. Quantitative comparison to van der Vegt's force field shows the Hofmeister swap at an earlier degree of deprotonation as well as bigger amounts of sodium bound at highly charged surfaces. In addition, contact ion pairs dominate the interaction with arachidates, which is in disagreement with both van der Vegt's force field and the experiment.

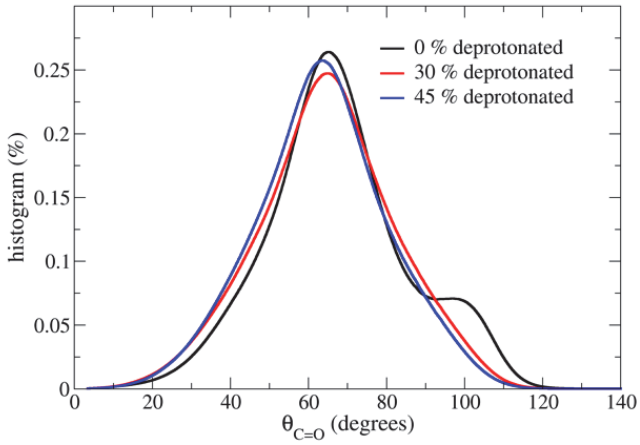

Figure S5 – Orientation of the carbonyl group of the arachidic acid as a function of deprotonation of the Langmuir monolayer determined from all-atom MD simulations using the charmm36 force field. Average angles between the carbonyl group and the surface normal are depicted in black (fully uncharged surface), red (30 % deprotonated surface), and blue (45 % deprotonated surface).

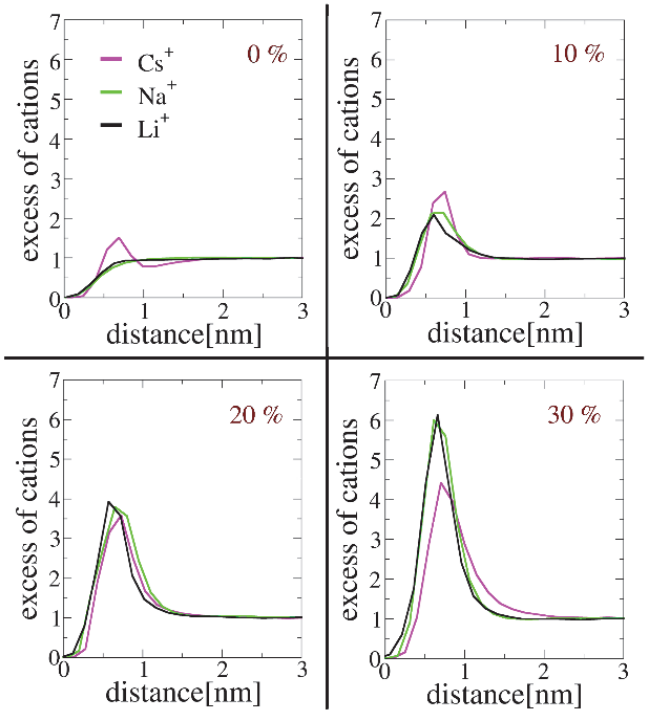

Figure S6 – MD simulations showing the interactions of cations with fully protonated (0%), 10 %, 20 %, and 30 % deprotonated surfaces of arachidic acid. Normalized number densities are calculated along the z-axis, where 0 is the position of the water/acid interface and 3 nm is the bulk solution. An OPLS force field was used for the monolayer and a scaled charges force field for the ions.

5. Langmuir isotherms of dAA. Effect of ion concentration and pH.

The surface pressure vs molecular area isotherms remained very much the same for all the different subphase conditions studied in this work, which included varying the pH from 4.5 up to 9.0, as well as the identity and concentration of the alkali metal salts (NaCl, LiCl, and CsCl). Examples are shown in Figure S7, were for different pH and salts the isotherms overlapped within an error ±0.5 Å^2. This is in stark contrast to the case of having divalent ions in the subphase,[22] or for pH>11,[23] where the isotherms change significantly. In the VSF measurements the average area per molecule at a surface pressure of 20 mN/m remained equal to ~20 Å^2 for all cases. Consequently, the nature of the monovalent alkali chloride salt does not affect the packing of the monolayer.

Note that although the isotherms measured at pH 9 overlapped within the error range, a small difference in the slope of the tilted condensed phase was observed depending on the nature of the electrolyte. The largest slopes was observed for Li+, which forms a contact ion pair with the carboxylate as discussed in the article.

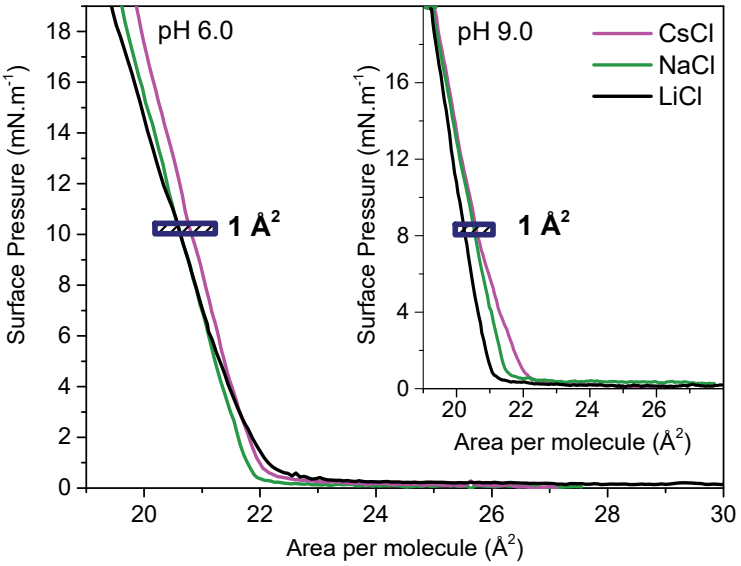

Figure S7 – Langmuir isotherms of a dAA monolayer on a 1M subphases of NaCl, LiCl, and CsCl at pH 6 and 22°C. Equivalent isotherms for pH 9 are shown as an inset.

6. VSF spectra in the CD stretching region collected at the SPS and PPP polarization combinations.

The VSF spectra of the alkyl chain of the deuterated arachidic acid in a tilted condensed phase (20 mN/m) on a 1M NaCl pH6 subphase, collected under the polarization combinations SSP, SPS and PPP is shown in Figure S8.

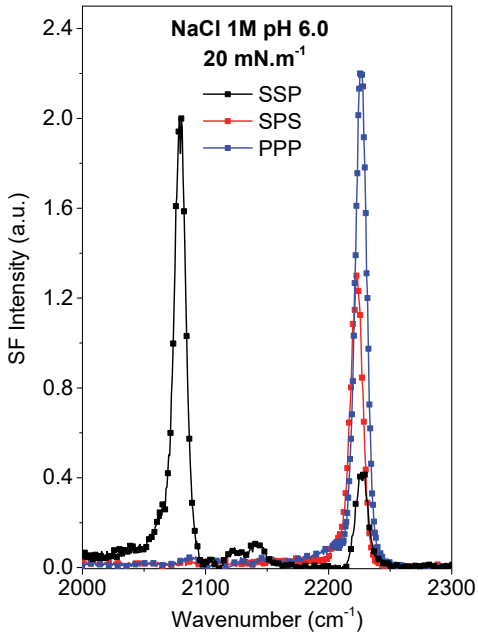

Figure S8 – VSF spectra in the CD stretching region of dAA on a 1 M NaCl, pH6 subphase collected in the SSP (*black*), SPS (*red*) and PPP (*blue*) polarization combinations. Note that the asymmetric CD_3 stretch at ~2217 cm^{-1} dominate the SPS and PPP spectra.

7. Orientational analysis of the C=O bond.

An orientational analysis of the carbonyl band was performed to further understand the origin of the observed changes in SF signal intensity upon deprotonation, and to determine the actual orientation of the C=O bond at the interface.[24-28] The procedure for a carbonyl group was described in detail in a previous publication, and here we follow a similar approach.[29] The C=O is treated as a first approximation as having a $C_{\infty v}$ symmetry, which implies that out of the 27 elements of the hyperpolarizability tensor only 2 independent elements remain: $\beta^{(2)}_{ccc}$; $\beta^{(2)}_{aac} = \beta^{(2)}_{bbc}$, where a, b, and c correspond to the spatial coordinates of the molecular frame, with c in the direction of the bond. To determine the ratio between the two independent hyperpolarizability elements we make use of the Raman depolarization ratio of the carbonyl measured above (section 2 in SI):

$$r = \frac{\beta_{aac}}{\beta_{ccc}} = \frac{\alpha_{aa}}{\alpha_{cc}} \qquad [S16]$$

Where the parameter r is related to the Raman depolarization ratio (ρ) by:

$$\rho = \frac{3}{4}\left[1 + \frac{5}{4}\left(\frac{2r+1}{r-1}\right)^2\right]^{-1} \qquad [S17]$$

From the molecular to the laboratory frame

The hyperpolarizability elements in the molecular frame are transformed into the laboratory coordinates (x, y, z) using Euler rotation transformation matrices. At isotropic (in the plane) interfaces the hyperpolarizability are averaged over the azimuthal angles. The non-linear susceptibility can be expressed as a function of the hyperpolarizability, where only the tilt angle ($\theta_{C=O}$) remains.

$$\chi_{YYZ} = \frac{N}{\varepsilon_0}\langle\beta_{YYZ}\rangle = \frac{1}{2}\frac{N}{\varepsilon_0}\beta_{ccc}\left[(r+1)\langle\cos\theta\rangle + (r-1)\langle\cos^3\theta\rangle\right] \qquad [S18]$$

$$\chi_{YZY} = \frac{N}{\varepsilon_0}\langle\beta_{YZY}\rangle = \frac{1}{2}\frac{N}{\varepsilon_0}\beta_{ccc}(1-r)\left(\langle\cos\theta\rangle - \langle\cos^3\theta\rangle\right)$$

$$\chi_{ZZZ} = \frac{N}{\varepsilon_0}\langle\beta_{ZZZ}\rangle = \frac{N}{\varepsilon_0}\beta_{ccc}\left[r\langle\cos\theta\rangle + (1-r)\langle\cos^3\theta\rangle\right]$$

Two distribution functions were assumed for the tilt orientational averaging: a delta distribution (δ) and the more realistic Gaussian distribution function (see Figure 3d in article):

$$\langle f(\theta)\rangle = \frac{1}{\sigma\sqrt{2\pi}}\int_0^{\pi} f(\theta)\exp\left(-\frac{(\theta-\theta_0)^2}{2\sigma^2}\right)\sin\theta.d\theta \qquad [S19]$$

Where θ_0 refers to the mean orientation angle, σ^2 to the variance and $f(\theta)$ to the averaging function. A standard deviation of 15° has been used in our calculation (see Figure 3d in article).

Finally, to take into account the intensity variations associated to our experimental geometry the Fresnel factor were calculated (Equations S20 to S25). The angles of incidence for the visible and IR beams are 70°, and 55°, respectively. The refractive indexes of the bulk incident phase (n_1, air) were trivially set to 1, while for the bulk liquid phase (n_2) those from pure water at the corresponding frequencies were used.[30] Further, the "refractive indexes" for the interfacial thin polarization sheet (n') were arbitrarily set to 1.25.[9]

$$\chi^{(2)}_{\text{eff, SSP}} = L_{yy}(\omega_{SF})\, L_{yy}(\omega_{vis})\, L_{zz}(\omega_{IR})\, \sin(\theta_{IR})\, \chi^{(2)}_{yyz} \quad [S20]$$

$$\chi^{(2)}_{\text{eff, SPS}} = L_{yy}(\omega_{SF})\, L_{zz}(\omega_{vis})\, L_{yy}(\omega_{IR})\, \sin(\theta_{vis})\, \chi^{(2)}_{yzy} \quad [S21]$$

$$\begin{aligned}\chi^{(2)}_{\text{eff, PPP}} = {} & -L_{xx}(\omega_{SF})\, L_{xx}(\omega_{vis})\, L_{zz}(\omega_{IR})\, \cos(\theta_{SF})\, \cos(\theta_{vis})\, \sin(\theta_{IR})\, \chi^{(2)}_{YYZ} \\ & - L_{xx}(\omega_{SF})\, L_{zz}(\omega_{vis})\, L_{xx}(\omega_{IR})\, \cos(\theta_{SF})\, \sin(\theta_{vis})\, \cos(\theta_{IR})\, \chi^{(2)}_{YZY} \\ & + L_{zz}(\omega_{SF})\, L_{xx}(\omega_{vis})\, L_{xx}(\omega_{IR})\, \sin(\theta_{SF})\, \cos(\theta_{vis})\, \cos(\theta_{IR})\, \chi^{(2)}_{zxx} \\ & + L_{zz}(\omega_{SF})\, L_{zz}(\omega_{vis})\, L_{zz}(\omega_{IR})\, \sin(\theta_{SF})\, \sin(\theta_{vis})\, \sin(\theta_{IR})\, \chi^{(2)}_{zzz}\end{aligned} \quad [S22]$$

$$L_{xx}(\omega_n) = \frac{2\, n_1(\omega_n)\, \cos(\gamma_n)}{n_1(\omega_n)\cos(\gamma_n) + n_2(\omega_n)\cos(\theta_n)} \quad [S23]$$

$$L_{yy}(\omega_n) = \frac{2\, n_1(\omega_n)\, \cos(\theta_n)}{n_1(\omega_n)\cos(\theta_n) + n_2(\omega_n)\cos(\gamma_n)} \quad [S24]$$

$$L_{zz}(\omega_n) = \frac{2\, n_2(\omega_n)\, \cos(\theta_n)}{n_1(\omega_n)\cos(\gamma_n) + n_2(\omega_n)\cos(\theta_n)} \left(\frac{n_1(\omega_n)}{n'(\omega_n)} \right)^2 \quad [S25]$$

where θ_n and γ_n are the angles of incidence and refraction, respectively.

The intensity of the SF signal SSP, SPS, and PPP are proportional to the square of the corresponding effective non-linear susceptibility. To determine the tilt angle ($\theta_{C=O}$) we compare the ratio of the theoretical curves that model the changes in intensity as a function of the tilt angle, with our experimentally determined amplitudes under different polarization combinations (i.e. SSP, PPP and SPS).

8. Fitting of the VSFS spectra

The spectra were fitted using a convolution of Gaussian and Lorentzian line shapes as presented in Equation 1 in the main text. The fitted amplitude of the symmetric carboxylate band was used to calculate the degree of deprotonation of the monolayer having as reference the expected amplitude for a fully deprotonated monolayer at pH 13.[23] Figure S9 shows the fitted curve of the dAA on a 1 M LiCl subphase taken from Figure 2a in the paper. The spectra were fitted using the 8 vibrational contributions as summarized in Table S4. Due to the coherent nature of the SF generation, information is also contained in the phase of the signal, given by the sign of the amplitude. Opposite signs, typically reveal an opposite net polar orientation of the chemical functional group.

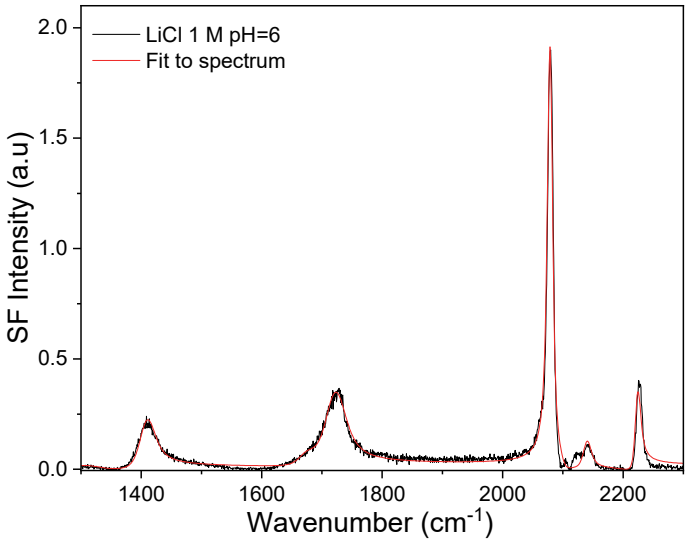

Figure S9 – VSF spectrum in the SSP polarization combination of a dAA monolayer on a 1 M LiCl subphase at pH 6.0 (*black line*), and its fitted curve (*red line*).

Table S4 – Fitting parameters for the spectrum shown in Figure S9. ω_i, Γ_i, σ_i, and A_i correspond to the frequency of vibration, the homogeneous and inhomogeneous broadening, and the amplitude, respectively. The values indicated with a star (*) have been fixed during the fitting procedure. The non-resonant background was A_{NR} = -0.13 ±0.01.

Mode	ω_i (cm^{-1})	Γ_i (cm^{-1})	σ_i (cm^{-1})	SSP, A_i
C–O	1320 ± 10	10±4	18±4	-2±1
ν_s (COO^-)	1408 ±1	8*	8*	5.6 ±0.2
OH (bend.)	1670 ±10	8	7.5	-3.6 ±0.4
C=O (stretch)	1719±4.0	10	11	9.1±0.3
ν_s (CD_3)	2077 ±1	3.5	2.7	-6.2 ±0.2
ν_s (CD_2)	2100*	3*	3*	0.5 ±0.3
Fermi (CD_3)	2139 ± 3	4*	4*	2 ± 1
ν_a (CD_3)	2222 ±1	2.9	2.9	2.5 ±0.2

Table S5 shows the fitted parameters used for the orientation analysis of the carbonyl band (Figure 3 in paper). The SSP over SPS intensity ratio for the C=O band varies upon deprotonation from ~1.6 in pure water, to ~2.5 in 500 mM NaCl. According to the orientational analysis theoretical curves (Figure 3d), the increase in the SSP / SPS ratio confirms the change of orientation, with the carbonyl tilting closer to the surface normal as the monolayer deprotonates. Note that the fitting amplitudes need to be squared in order to compare them with the values in the theoretical curves, which are shown in the main text as a ratio of intensities (Figure 3d).

Table S5 – Fitting parameters of the VSF spectra of Figure 3. Only the vibrational modes relevant to the orientational analysis are presented.

dAA on pure water subphase – Figure 3a

Mode	**ω_i (cm^{-1})**	**Γ_i (cm^{-1})**	**σ_i (cm^{-1})**	**SSP, A_i**	**SPS, A_i**
C–O		10±4	18±4	-6.2±0.2	0
ν_s (COO^-)	1408	-	-	0	0
ν_a (COO^-)	1315 ± 7	-	-	0	0
OH (bend.)	1670±10	8	7.5±2.5	-4.6±0.5	-2.9±0.1
C=O (stretch)	1715±4	19.5	8.6	10.7±0.1	8.6±0.1
A_{NR}				-0.14	-0.1

dAA on NaCl 100 mM pH 6.0 – Figure 3b

Mode	**ω_i (cm^{-1})**	**Γ_i (cm^{-1})**	**σ_i (cm^{-1})**	**SSP, A_i**	**SPS, A_i**
C–O	1315 ± 7	10±4	18±4	-4±1	0
ν_s (COO^-)	1407 ± 1	8.0	8.0	4.7±0.1	0
ν_a (COO^-)	-	-	-	0	0
OH (bend.)	1670 ± 10	8.0	7.5±2.5	-3.2±0.4	-2.1±0.1
C=O (stretch)	1720 ± 3	10	11	8.9±0.2	5.9±0.1
A_{NR}				-0.13	-0.1

dAA on NaCl 500 mM pH 6.0 – Figure 3c

Mode	**ω_i (cm^{-1})**	**Γ_i (cm^{-1})**	**σ_i (cm^{-1})**	**SSP, A_i**	**SPS, A_i**
C–O	1320 ± 15	10±4	18±4	-1.5±1	0
ν_s (COO^-)	1407 ± 1	8.0	8.0	6.8±0.1	0
ν_a (COO^-)	1535 ± 3	9	17±2	0	2.0±0.2
OH (bend.)	1670 ± 10	8.0	7.5	-3.5±0.3	-2.1±0.1
C=O (stretch)	1720 ± 3	10	11	8.9±0.2	5.7±0.1
A_{NR}				-0.13	-0.03

9. **Water at charged interfaces: $\chi_s^{(2)}$ and $\chi^{(3)}$ response.**

The SF response can originate from water molecules in the immediate surface region ($\chi_s^{(2)}$) and/or in the diffuse double layer that extends further into the bulk ($\chi^{(3)}$ term).[31-33] The intensity of the SF signal (I_{SF}) is proportional to:

$$I_{SF} \propto I_{vis} I_{IR} \left| \chi_s^{(2)} + \chi^{(3)} \int_0^{+\infty} E_{DC}(z) e^{i\Delta k_z z} dz \right|^2 \approx I_{vis} I_{IR} \left| \chi_s^{(2)} + \chi^{(3)} \psi_0 \frac{\kappa}{\kappa - i\Delta k_z} \right|^2 \quad [S26]$$

where I_{vis} and I_{IR} are the visible and IR beam intensities, respectively; $\chi^{(3)}$ is the effective third-order susceptibility, which is dominated by water molecules perturbed by the exponentially decaying surface electric field, $E_{DC}(z)$; Δk_z is a phase factor accounting for the limited coherence length of the SF process, and κ^{-1} is the Debye screening length. In the geometry of our experiments $\Delta k_z^{-1} \approx 51$ nm. In the model shown as a red line in Figure 6b (main text) the $\chi_s^{(2)}$ was set to be equal to -0.12 (1-2α) and $\chi^{(3)} = 1$, where α is the degree of deprotonation of the monolayer.[23] The decrease of $\chi_s^{(2)}$ with degree of deprotonation is justified since it was established that it primarily originates from water molecules interacting with the uncharged carboxylic acid moiety, which relative proportion decreases as the monolayer deprotonates (the prefactor of 2 multiplying α was selected as it gave a better fit to the experimental data at low ionic strengths).[23] Actually, at 1 M the OH spectral features are almost identical to those for pure water, only that the absolute intensities are reduced by approximately 50%. This suggests that at high ionic strengths the last term in equation S26 vanishes. Since the surface potential is not zero, the direct implication is that the value of $\chi^{(3)}$ does not remain constant and equal to 1, but decreases with ionic strength, reaching a value of almost zero at 1 M NaCl. In other words, the value of $\chi^{(3)}$ is no longer equivalent to the bulk value,[34, 35] but decreases as the condensed surface layer of hydrated ions, predicted by the MPB model, is formed. Note that the surface potential employed in Equation S26 was determined from the experimental surface charge using the modified PB model. Consequently, in the absence of any additional information like the surface charge of the monolayer determined in this study, extracting surface potential values from the intensities of the OH stretching bands at high ionic strengths could be questionable and subject to gross misinterpretations.

References

1. W. Hua, D. Verreault, E. M. Adams, Z. Huang and H. C. Allen, *The Journal of Physical Chemistry C*, 2013, **117**, 19577-19585.
2. Z. Huang, W. Hua, D. Verreault and H. C. Allen, *The Journal of Physical Chemistry A*, 2013, **117**, 13412-13418.
3. G. B. Deacon and R. J. Phillips, *Coord. Chem. Rev.*, 1980, **33**, 227-250.
4. J. E. Tackett, *Appl. Spectrosc.*, 1989, **43**, 483-489.
5. C. Y. Tang and H. C. Allen, *J. Phys. Chem. A*, 2009, **113**, 7383-7393.
6. G. Anderegg, *Critical Survey of Stability Constants of EDTA Complexes: Critical Evaluation of Equilibrium Constants in Solution: Stability Constants of Metal Complexes*, Elsevier Science, 2013.
7. E. Tyrode and J. F. D. Liljeblad, *J. Phys. Chem. C*, 2013, **117**, 1780-1790.
8. C. M. Johnson, E. Tyrode, S. Baldelli, M. W. Rutland and C. Leygraf, *The Journal of Physical Chemistry B*, 2005, **109**, 321-328.
9. E. Tyrode and J. Hedberg, *J. Phys. Chem. C*, 2012, **116**, 1080-1091.
10. D. F. Evans and H. Wennerström, *The Colloidal Domain: Where Physics, Chemistry, Biology, and Technology Meet, 2nd*, 1998.
11. G. Gouy, *C. R. Seances Acad. Sci.*, 1909, **149**, 654-657.
12. D. L. Chapman, *Lond. Edinb. Dubl. Phil. Mag.*, 1913, **25**, 475-481.
13. K. Dill and S. Bromberg, *Molecular Driving Forces. Statistical Thermodynamics in Biology, Chemistry, Physics, and Nanoscience*, Garland Science, New York, 2nd edn., 2010.
14. E. Pezron, P. M. Claesson, J. M. Berg and D. Vollhardt, *Journal of Colloid and Interface Science*, 1990, **138**, 245-254.
15. I. Borukhov, D. Andelman and H. Orland, *Physical Review Letters*, 1997, **79**, 435-438.
16. M. S. Kilic, M. Z. Bazant and A. Ajdari, *Phys. Rev. E*, 2007, **75**, 021502.
17. I. Borukhov, D. Andelman and H. Orland, *Electrochimica Acta*, 2000, **46**, 221-229.
18. B. Hess and N. F. A. van der Vegt, *Proc. Natl. Acad. Sci.*, 2009, **106**, 13296-13300.
19. R. A. Robinson and R. H. Stokes, *Electrolyte Solutions: Second Revised Edition*, Dover Publications, 2002.
20. E. Pluhařová, P. E. Mason and P. Jungwirth, *J. Phys. Chem. A*, 2013, **117**, 11766-11773.
21. M. Kohagen, P. E. Mason and P. Jungwirth, *J. Phys. Chem. B*, 2016, **120**, 1454-1460.
22. E. Le Calvez, D. Blaudez, T. Buffeteau and B. Desbat, *Langmuir*, 2001, **17**, 670-674.
23. E. Tyrode and R. Corkery, *J. Phys. Chem. C*, 2018, **122**, 28775-28786.
24. C. Hirose, N. Akamatsu and K. Domen, *Appl. Spectrosc.*, 1992, **46**, 1051-1072.
25. X. Zhuang, P. B. Miranda, D. Kim and Y. R. Shen, *Physical Review B: Condensed Matter*, 1999, **59**, 12632-12640.
26. H.-F. Wang, W. Gan, R. Lu, Y. Rao and B.-H. Wu, *International Reviews in Physical Chemistry*, 2005, **24**, 191-256.
27. G. R. Bell, Z. X. Li, C. D. Bain, P. Fischer and D. C. Duffy, *J. Phys. Chem. B*, 1998, **102**, 9461-9472.
28. E. Tyrode, C. M. Johnson, M. W. Rutland, J. P. R. Day and C. D. Bain, *J. Phys. Chem. C*, 2007, **111**, 316-329.
29. E. Tyrode, C. M. Johnson, S. Baldelli, C. Leygraf and M. W. Rutland, *The Journal of Physical Chemistry B*, 2005, **109**, 329-341.
30. G. M. Hale and M. R. Querry, *Applied Optics*, 1973, **12**, 555-563.
31. G. Gonella, C. Lütgebaucks, A. G. F. de Beer and S. Roke, *J. Phys. Chem. C*, 2016, **120**, 9165-9173.
32. S. Ong, X. Zhao and K. B. Eisenthal, *Chem. Phys. Lett.*, 1992, **191**, 327-335.
33. Y.-C. Wen, S. Zha, X. Liu, S. Yang, P. Guo, G. Shi, H. Fang, Y. R. Shen and C. Tian, *Phys. Rev. Lett.*, 2016, **116**, 016101.
34. X. L. Zhao, S. W. Ong and K. B. Eisenthal, *Chem. Phys. Lett.*, 1993, **202**, 513-520.
35. T. Joutsuka, T. Hirano, M. Sprik and A. Morita, *Phys. Chem. Chem. Phys*, 2018, **20**, 3040-3053.